Prospective two orders of magnitude enhancement in direct magnetic coupling of a single-atom spin to a circuit resonator

Bahman Sarabi,[1, 2] Peihao Huang,[1, 2] and Neil M. Zimmerman[1]

[1]*National Institute of Standards and Technology, Gaithersburg, MD 20899, USA*
[2]*Joint Quantum Institute, University of Maryland, College Park, Maryland 20742, USA*
(Dated: February 9, 2017)

We report on the challenges and limitations of direct coupling of the magnetic field from a circuit resonator to an electron spin bound to a donor potential. We propose a device consisting of a lumped-element superconducting resonator and a single donor implanted in enriched ^{28}Si. The resonator, in contrast to coplanar waveguide resonators, includes a nano-scale spiral inductor to spatially focus the magnetic field from the photons within. The design promises approximately two orders of magnitude increase in the local magnetic field, and thus the spin to photon coupling rate g, compared to the estimated coupling rate to coplanar transmission-line resonators. We show that by using niobium (aluminum) as the resonator's superconductor and a single phosphorous (bismuth) atom as the donor, a coupling rate of $g/2\pi$=0.24 MHz (0.39 MHz) can be achieved in the small photon limit. For this truly linear cavity quantum electrodynamic system, such enhancement in g is sufficient to enter the strong coupling regime.

Silicon-based spin qubits, including gate-defined quantum dot [1–3] and single-atom [4, 5] devices, use the spin degree of freedom to store and process quantum information, and are promising candidates for future quantum electronic circuits. The electronic or nuclear spin is well decoupled from the noisy environment, resulting in extremely long coherence times [6–8] desirable for fault-tolerant quantum computing. Single-atom spin qubits offer additional advantages over quantum dot qubits such as longer coherence due to strong confinement potentials, and are expected to have better reproducibility by nature. Therefore, it is no surprise that silicon-based single-atom spin qubits hold the record coherence times of any solid state single qubit [10]. However, this attractive isolation from sources of decoherence comes at the price of relatively poor coupling to the control and readout units. This causes relatively long qubit initialization times, degraded readout fidelity, and weak spin-spin coupling for multi-qubit gate operations [10].

One simple way to increase the coupling rate is to increase the ac field from the external circuit. In this regard, superconducting circuit resonators are attractive due to their relatively large quality factors, ease of coupling to other circuits, their capability of generating ac fields by carrying relatively large currents and monolithic integration with semiconductor devices.

For many years, superconducting microwave resonators have had extensive applications that range from superconducting qubit manipulation [11] and inter-qubit coupling [12] to dielectric characterization [13]. One of the most commonly used superconducting quantum computing architectures is one based on cavity quantum electrodynamics (cQED) [6], in which a 2D (circuit based) or 3D cavity is employed to initialize, manipulate and readout the superconducting qubit. Superconducting circuit cavities have not yet found a similar prevalence in spin qubit circuits due to the fact that the magnetic field of a

typical superconducting resonator and the spin magnetic moment are relatively small, leading to an insufficient spin-photon coupling strength for practical purposes.

Several methods have been proposed to enhance the coupling of a single spin to a photon within a superconducting circuit resonator. It is easier to couple a photon to quantum dot spin qubits than to single-atom spins because in the former, the spin dynamics can be translated into an electric dipole interacting with resonator's electric field [15–17]. Such architectures, however, require hybridization of the spin states with charge states, imposing charge noise on the spin and thus affecting its coherence. On the other hand, direct magnetic coupling of coplanar transmission-line resonators to donor electrons in silicon [18, 19] and diamond nitrogen-vacancy centers [20, 21] can only achieve a maximum single-spin coupling rate of a few kHz. This relatively weak coupling makes practical spin qubit initialization, manipulation and readout very challenging. For the single-atom spin qubits, indirect coupling to a resonator via superconducting qubits [22, 23] can enhance the coupling, but imposes nonlinearity on the circuit complicating cQED analysis, and also introduces loss from Josephson junction tunnel barriers [24, 25] and magnetic flux noise [26].

In this paper, we show that replacing the coplanar resonator with a lumped-element circuit resonator that includes a spiral inductor, can lead to a dramatic enhancement in the spin-photon magnetic coupling rate g of approximately two orders of magnitude. As we will discuss, this improvement is a result of employing a lumped-element trilayer design along with nano-scale spiral loops which effectively localize the resonator's magnetic field at the location of the spin, eliminating the need for an Oersted line [27]. We also show that this coupling rate is enough to take the spin-resonator hybrid system to the strong coupling regime, where g is larger than or approximately equal the resonator de-
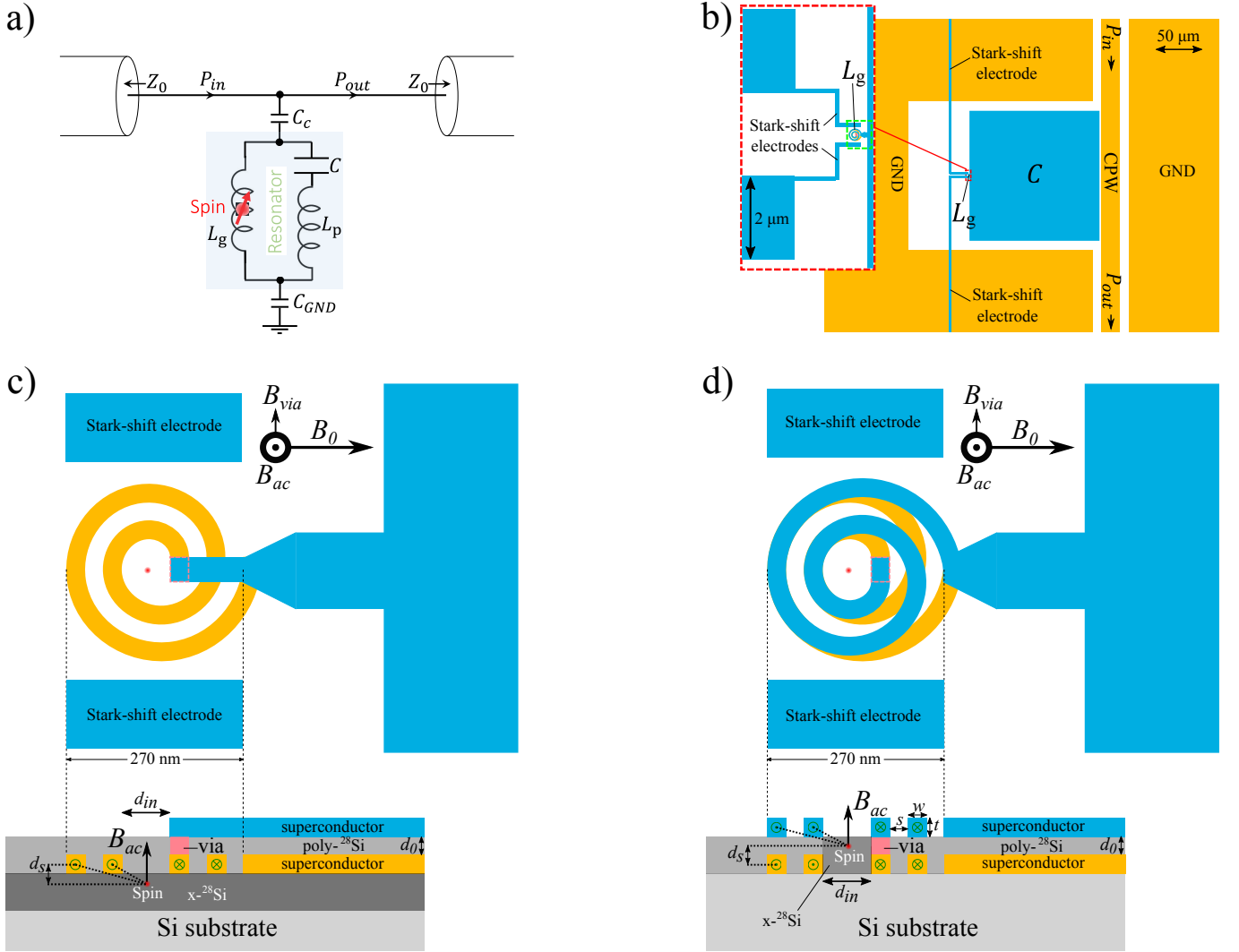
FIG. 1. (a) Schematic of the circuit showing the resonator coupled to the coplanar waveguide (CPW) via C_c, representing the effective CPW coupling to resonator's capacitor C. C_{GND} is the floating resonator's capacitance to ground. P_{in}, P_{out}, L_g and L_p show the microwave input power, output power, geometric inductance and the parasitic inductance of the resonator circuit, respectively. This arrangement of L_g and L_p is valid in the limit of $C \gg C_c, C_{GND}$. (b) Layout of the device showing resonator's capacitor C and inductor L. Blue and orange show the top and bottom superconducting layers, respectively. The area within the red dashed square is magnified. The spiral inductor within the green dashed square is further magnified to show the following geometries (red dot represents the spin): (c) single spiral (1S) with $d_s = 25$ nm and (d) double spiral (2S) with $d_s = 27.5$ nm. Dimensions are $w = s = t = d_{in}/2 = 30$ nm, compatible with standard electron beam lithography, and $d_0 = 25$ nm. The crystalline ^{28}Si (x-^{28}Si) growth is required only in the volume surrounding the spin, and amorphous or polycrystalline Si is acceptable everywhere else. The relatively weak magnetic field $\mathbf{B}_{via}$ (directions shown represent magnetic fields at the location of the spin) from the via determines the best choice for the direction of the static magnetic field, $\mathbf{B}_0 \parallel (\mathbf{B}_{via} \times \mathbf{B}_{ac})$, where $\mathbf{B}_{ac}$ is the magnetic field from the spiral inductor. This ensures that the total ac field is perpendicular to $\mathbf{B}_0$. Current within the spiral is shown by green in- or out of plane vectors.

cay rate κ. Due to the relatively small total inductance L_{tot} in this device, coplanar interdigitated capacitances are insufficient to achieve the desired operation frequency $\omega_0 = 1/\sqrt{L_{tot}C}$. Therefore, the proposed device geometry, compatible with standard micro- and nanofabrication techniques, includes a trilayer (parallel-plate) capacitor with a deposited insulating layer. Trilayer capacitors, however, give rise to a lower resonator Q than that of a typical coplanar geometry. Nevertheless, as our calculations show, the increase in g resulted from employing a trilayer lumped-element design is large enough to overcome the limited Q, allowing for strong spin-photon coupling.

The lossless dynamics of a spin-$\frac{1}{2}$ system with spin transition frequency ω_s coupled with rate g to a cavity resonant at ω_0, is described by the Jaynes-Cummings

Hamiltonian, $\mathcal{H} = \hbar\omega_0(\hat{a}^\dagger\hat{a} + 1/2) + (1/2)\hbar\omega_s\hat{\sigma}^z + \hbar g(\hat{a}^\dagger\hat{\sigma}^- + \hat{\sigma}^+\hat{a})$ [28]. Here, a and σ are photon and spin operators, respectively. The spin-photon magnetic coupling rate is obtained as $g = g_e\mu_B B_{ac,0}\langle g|\hat{S}_x|e\rangle/\hbar$ where $g_e \simeq 2$ is the electron g-factor, μ_B is the Bohr magneton, and $B_{ac,0} = \langle n = 0|\hat{B}_{ac}^2|n = 0\rangle^{1/2}$ is the root mean square (RMS) local magnetic field at zero photons on resonance ($n = 0$). $|g\rangle$ and $|e\rangle$ are the ground and excited spin states, respectively, that couple to the microwave field. Finally, the spin rotation speed can be enhanced with a larger local RMS magnetic field $B_{ac} = \langle n|\hat{B}_{ac}^2|n\rangle^{1/2}$ for any arbitrary n.

The schematic and layout of the proposed circuit are shown in Figs. 1(a) and 1(b), respectively, where a LC resonator is capacitively coupled to a coplanar waveguide (CPW) and the donor is within the resonator's deliberate inductor. The capacitance is provided using a trilayer capacitor. The RMS current through the inductor at an average photon number $\bar{n}$ on resonance is $I_{ac} = \sqrt{(\bar{n} + 1/2)\hbar\omega_0/L_{tot}}$, where ω_0 is the resonance frequency and L_{tot} denotes the total inductance within the resonator circuit. Since the desired ac magnetic field from the loop(s) is proportional to I_{ac}, it is clear that the inductance must be minimized and photon frequency must be maximized for the maximum magnetic field. Therefore, it is necessary to study the sources of inductance and obtain operation frequency limitations.

The total inductance within the resonator circuit is obtained as $L_{tot} = L_g + L_p$, where L_g is the geometric inductance of the spiral inductor and is the only inductance within the circuit that gives rise to the RMS magnetic field B_{ac} localized at the spin. The parasitic inductance L_p arises from the kinetic inductance, coupling inductance, self-inductance of the capacitor, inductance of the uncovered areas of the capacitor plates and the kinetic inductance within the capacitor plates. Since L_p does not create any magnetic fields at the location of the spin and only limits I_{ac} through L_{tot}, we want to minimize it. For a better understanding of the dependence of g on the number N_{loops} of the spiral loops, a naive picture may be helpful to the reader. To the first order for $N_{loops} = 1$, $I_{ac} \propto 1/\sqrt{L_g + L_p}$, and $L_g \propto N_{loops}^2 \ln(N_{loops})$, and $B_{ac,0}, g \propto I_{ac}\ln(N_{loops})$, but L_p is a weaker function of N_{loops} than L_g. This suggest that by increasing N_{loops}, $B_{ac,0}$ and hence g increase up to a point where L_g approaches L_p, and I_{ac} begins to drop as N^α, with $\alpha < -1$. Employing a lumped element design provides the required flexibility to reach this optimum L_g and the corresponding N_{loops}.

In order to obtain an accurate estimation of L_g and L_p, we performed calculations as well as software simulations. The details of our analysis is included in the supplementary material. We study two different device geometries, one using a single spiral (1S) inductor and the other using a double spiral (2S) inductor shown in Figs.
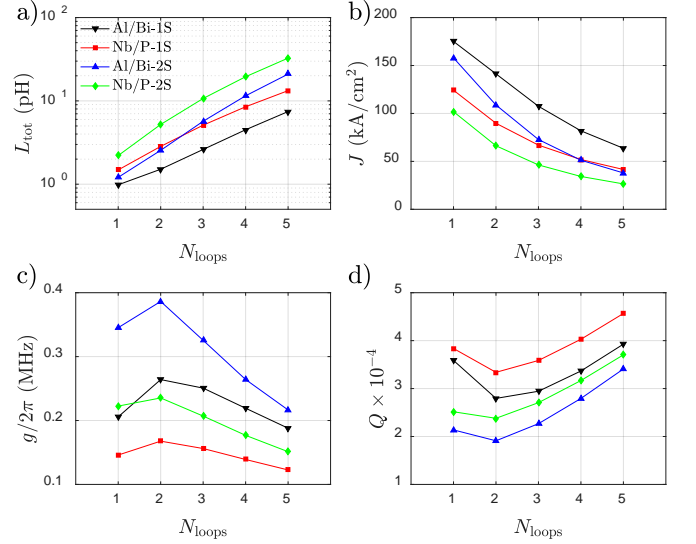

FIG. 2. Plots of the (a) total inductance, (b) current density through the spiral inductor, (c) spin-photon coupling rate and (d) the required resonator quality factor $Q \equiv \omega_0/g$ to allow strong spin-photon coupling versus the number of spiral loops N_{loops} for different combinations of materials and geometries, i.e. superconducting aluminum and Bismuth donor (Al/Bi), superconducting niobium and phosphorous donor (Nb/P), single spiral (1S) and double spiral (2S) geometries.

1(c)-(d). N_{loops} refers to the number of loops in a single spiral layer regardless of the geometry, e.g., $N_{loops} = 2$ for both Figs. 1(c) and 1(d). In general, the 1S design is expected to be easier to fabricate at the expense of smaller g compared to the 2S geometry. For each of these geometries, we study two sets of materials, one that uses niobium as superconductor and phosphorous as the donor (Nb/P) and one with aluminum as superconductor and bismuth as donor (Al/Bi). This results in four configurations under consideration, i.e. Al/Bi-1S, Al/Bi-2S, Nb/P-1S and Nb/P-2S. Figure 2(a) shows L_{tot} from calculations and simulations as a function of N_{loops} for all four configurations.

Fabrication is considered to be slightly better established with Al, whereas Nb has a critical magnetic field of $B_{c1,Nb} = 0.2$ T, which is the highest B_{c1} among the single-element superconductors. Through the Zeeman effect, for the Nb/P set, the uncoupled electron spin-up ($|\uparrow\rangle$) and spin-down ($|\downarrow\rangle$) states are split by the photon frequency $\omega_0/2\pi = 5.6$ GHz corresponding to $B_0 = \hbar\omega_0/g_e\mu_B \simeq B_{c1,Nb}$. For the Al/Bi set, we consider operating at $B_0 < 10$ mT below the critical magnetic field of Al, and use the splitting of the spin multiplets ($\omega_0/2\pi = 7.375$ GHz) of the Bi donor. These splittings arise from the strong hyperfine interaction between the electron ($S = 1/2$) and Bi nuclear spin ($I = 9/2$) [29], leading to a total spin F and its projection m_F along $\mathbf{B_0}$. By employing the $|F, m_F\rangle = |5, -5\rangle \leftrightarrow |4, -4\rangle$ transition corresponding to the largest $\hat{S}_x$ matrix element (0.47),

and a static magnetic field of $B_0 = 5$ mT, the multiplet degeneracy at $B_0 = 0$ is lifted by more than 20 MHz, enough to decouple the nearby transitions [9, 31].

Figure 2(b) shows the vacuum fluctuation's current density $J = (1/wt)I_{ac}|_{\bar{n}=0}$ for each configuration, where w and t are the width and thickness of the spiral traces, respectively (see Fig. 1(d)). Clearly, J stays far below the critical current values of Al ($J_c \sim 10^4$ kA/cm^2 [32]) and Nb ($J_c \sim 10^3$ kA/cm^2 [33]).

At the location of the spin, B_{ac} is approximated as the sum of the magnetic field from all loops, $i.e$, $B_{ac} = \sum_{\text{loops}} \mu_0 I_{ac}/2R'_{\text{loop}}$ where $R'_{\text{loop}} \equiv (d_{in}^2 + 4d_s^2)^{3/2}/2d_{in}^2$ is defined as a characteristic radius which accounts for the spin location with respect to the center of the loops and d_s denotes the spin displacement from this center (see Figs. 1(c)-(d)). Note that the assumption of current flowing in the center of the spiral conductor underestimates B_{ac}, $B_{ac,0}$ and g, because in reality the majority of current will flow closer to the superconductor-silicon interface due to the relatively large electric permittivity ($\epsilon_r = 12$) of silicon.

Increasing N_{loops} from 1 to 2 increases $B_{ac,0}$, but, for $N_{\text{loops}} > 2$, the competing effect of larger L_{tot} and R'_{loop} suppresses I_{ac} and lowers g. This effect is clearly demonstrated in Fig. 2(c) as the optimum $N_{\text{loops}} = 2$ for all four configurations, where the vacuum fluctuation's coupling rates for the Al/Bi-2S and Nb/P-2S configurations are obtained as $g/2\pi = 0.39$ MHz and 0.24 MHz, respectively. To the knowledge of the authors, these values are approximately two orders of magnitude larger than a previously proposed architecture [19]. As we will discuss in the remainder of this paper, this new regime of g can lead to significant improvements in spin qubit manipulation rates and readout fidelities, and potentially enables new experiments such as individual spin spectroscopy.

From the experimental point of view, a relatively simple first step is to implant one (or a few) donors inside the spiral and measure the spectrum in the small photon limit while the electron spin transitions are tuned across the resonator bandwidth. The advantage of incorporating N_s spins is that the collective coupling rate $g\sqrt{N_s}$ [18] yields more clear spin-resonator interaction features in the spectra for the first iteration of the device, as observed in other two-level system ensembles [34]. In our proposed device, tuning of the spin(s) can be performed using magnetic (Zeeman) or electric (Stark, see Fig. 1) fields, or a combination of both. The spectroscopy measurement can serve as a simple proof for entering the strong coupling regime. Furthermore, using the spectra and a theoretical model [35] based on the Jaynes-Cummings model, the spin-resonator coupling rate, spin coherence time and the resonator decay rate, as well as the spin electric field and magnetic field tunability can be extracted.

The condition for the system to enter the strong cou-

pling regime in the small photon limit is $Q \gtrsim \omega_0/g$, where $Q = \omega_0/\kappa$ and κ are resonator's total quality factor and total photon decay rate, respectively. Thanks to the relatively large spin-photon coupling rate, resonator Q's in the range of 10^4s are enough to take the system to the strong coupling regime for all four configurations (see Fig. 2(d)). In general, in the limit of low drive power and low temperature, trilayer resonators are significantly lossier than the coplanar resonators due to the fact that almost all the photon electric energy is stored within the parallel-plate capacitor dielectric containing defects. These defects act as lossy two-level fluctuators at small powers and low temperatures, and limit the resonator Q [25]. However, loss tangents as small as 10^{-5} have been measured for deposited amorphous hydrogenated silicon (a-Si:H) at single photon energies [36] promising resonator Q's of approximately 10^5. More recently, elastic measurements have indicated the absence of tunneling states in a hydrogen-free amorphous silicon film suggesting the possibility of depositing "perfect" silicon [37], promising even higher Q trilayer resonators using silicon as capacitor dielectric. Note that amorphous or polycrystalline Si, which have similar permittivities to crystalline Si, will only have to serve the purpose of confining electric field to avoid a large capacitor, and it is strongly preferred to implant the donor within the crystalline ^{28}Si to avoid fast decoherence [7]. From the fabrication point of view, it is easiest to use the same ^{28}Si film as the capacitor dielectric which, in general, will be in the polycrystalline form when deposited on the bottom capacitor plate (see Fig. 1(c-d)). It is noteworthy that using a trilayer design makes the resonator quality factor Q independent from the surrounding material as almost all the electric field is confined within the capacitor dielectric. This is useful for the integration of single electron devices that require lossy oxide layers.

We next briefly report the major single qubit gate operation parameters for the Nb/P-2S configuration (details of parameter derivations and qubit operation are included in the supplementary material). We can rapidly initialize by using the Purcell-limited zero-detuning relaxation time of $T_{1,init} = 2.3$ μs, many orders of magnitude shorter than the free spin relaxation. Effective initialization of spin systems using resonator coupling has been previously observed [9], and the 2-order of magnitude increase in g in our device promises a much faster initialization. For spin manipulation, we operate in a detuned regime, where the rotation speed with the maximum possible drive power is $f_{\text{rot}} = 29$ MHz, corresponding to $N_\pi > 10^5$ coherent π-rotations. In this regime, the spiral inductor's current density stays below J_c, similar to Fig. 2(b). For the spin readout, also performed in the detuned regime, a $\phi = 10°$ transmission phase difference depending on the spin state can be achieved. This phase difference is well above the measurement sensitivity usually considered to be $0.1°$, and suggests an extremely

high-fidelity readout.

In summary, we have proposed and designed a novel device that enhances the coupling of a single atom spin to the magnetic field of a circuit resonator by approximately 100 times compared to the previously proposed architectures that use coplanar transmission line resonators. This dramatic improvement is a result of using a lumped element resonator design and a spiral inductor geometry. We showed the possibility of entering the strong coupling regime necessary for practical purposes, *i.e.*, spectroscopic measurements and qubit realization. Using the principles of cavity quantum electrodynamics, we showed that this large g can lead to a significantly enhanced spin relaxation rate desired for qubit initialization, tens of megahertz spin rotation speed during manipulation without the need for an Oersted line, and superb dispersive readout sensitivity. Moreover, this architecture can be useful for coupling distant qubits using cavity photons for the realization of multi-qubit gates.

[1] R. Hanson, L. P. Kouwenhoven, J. R. Petta, S. Tarucha, and L. M. K. Vandersypen, Rev. Mod. Phys. **79**, 1217 (2007).

[2] D. Loss and D. P. DiVincenzo, Phys. Rev. A **57**, 120 (1998).

[3] J. R. Petta, A. C. Johnson, J. M. Taylor, E. A. Laird, A. Yacoby, M. D. Lukin, C. M. Marcus, M. P. Hanson, and A. C. Gossard, Science **309**, 2180 (2005).

[4] F. A. Zwanenburg, A. S. Dzurak, A. Morello, M. Y. Simmons, L. C. L. Hollenberg, G. Klimeck, S. Rogge, S. N. Coppersmith, and M. A. Eriksson, Rev. Mod. Phys. **85**, 961 (2013).

[5] J. J. Pla, K. Y. Tan, J. P. Dehollain, W. H. Lim, J. J. Morton, D. N. Jamieson, A. S. Dzurak, and A. Morello, Nature **489**, 541 (2012).

[6] K. Saeedi, S. Simmons, J. Z. Salvail, P. Dluhy, H. Riemann, N. V. Abrosimov, P. Becker, H.-J. Pohl, J. J. Morton, and M. L. Thewalt, Science **342**, 830 (2013).

[7] A. M. Tyryshkin, S. Tojo, J. J. Morton, H. Riemann, N. V. Abrosimov, P. Becker, H.-J. Pohl, T. Schenkel, M. L. Thewalt, K. M. Itoh, and S. A. Lyon, Nat. Mater. **11**, 143 (2012).

[8] M. Steger, K. Saeedi, M. L. W. Thewalt, J. J. L. Morton, H. Riemann, N. V. Abrosimov, P. Becker, and H.-J. Pohl, Science **336**, 1280 (2012).

[10] J. T. Muhonen, J. P. Dehollain, A. Laucht, F. E. Hudson, R. Kalra, T. Sekiguchi, K. M. Itoh, D. N. Jamieson, J. C. McCallum, A. S. Dzurak, and A. Morello, Nat. Nanotechnol. **9**, 986 (2014).

[10] D. D. Awschalom, L. C. Bassett, A. S. Dzurak, E. L. Hu, and J. R. Petta, Science **339**, 1174 (2013).

[11] A. Wallraff, D. I. Schuster, A. Blais, L. Frunzio, R.-S. Huang, J. Majer, S. Kumar, S. M. Girvin, and R. J. Schoelkopf, Nature **431**, 162 (2004).

[12] J. Majer, J. Chow, J. Gambetta, J. Koch, B. Johnson, J. Schreier, L. Frunzio, D. Schuster, A. Houck, A. Wallraff, *et al.*, Nature **449**, 443 (2007).

[13] B. Sarabi, A. N. Ramanayaka, A. L. Burin, F. C. Wellstood, and K. D. Osborn, Phys. Rev. Lett. **116**, 167002 (2016).

[6] A. Blais, R.-S. Huang, A. Wallraff, S. M. Girvin, and R. J. Schoelkopf, Phys. Rev. A **69**, 062320 (2004).

[15] K. Petersson, L. McFaul, M. Schroer, M. Jung, J. Taylor, A. Houck, and J. Petta, Nature **490**, 380 (2012).

[16] J. J. Viennot, M. C. Dartiailh, A. Cottet, and T. Kontos, Science **349**, 408 (2015).

[17] X. Hu, Y.-x. Liu, and F. Nori, Phys. Rev. B **86**, 035314 (2012).

[18] A. Imamoğlu, Phys. Rev. Lett. **102**, 083602 (2009).

[19] G. Tosi, F. A. Mohiyaddin, H. Huebl, and A. Morello, AIP Adv. **4**, 087122 (2014).

[20] Y. Kubo, F. R. Ong, P. Bertet, D. Vion, V. Jacques, D. Zheng, A. Dréau, J.-F. Roch, A. Auffeves, F. Jelezko, J. Wrachtrup, M. F. Barthe, P. Bergonzo, and D. Esteve, Phys. Rev. Lett. **105**, 140502 (2010).

[21] R. Amsüss, C. Koller, T. Nöbauer, S. Putz, S. Rotter, K. Sandner, S. Schneider, M. Schramböck, G. Steinhauser, H. Ritsch, J. Schmiedmayer, and J. Majer, Phys. Rev. Lett. **107**, 060502 (2011).

[22] Y. Kubo, C. Grezes, A. Dewes, T. Umeda, J. Isoya, H. Sumiya, N. Morishita, H. Abe, S. Onoda, T. Ohshima, V. Jacques, A. Dréau, J.-F. Roch, I. Diniz, A. Auffeves, D. Vion, D. Esteve, and P. Bertet, Phys. Rev. Lett. **107**, 220501 (2011).

[23] J. Twamley and S. D. Barrett, Phys. Rev. B **81**, 241202 (2010).

[24] R. W. Simmonds, K. M. Lang, D. A. Hite, S. Nam, D. P. Pappas, and J. M. Martinis, Phys. Rev. Lett. **93**, 077003 (2004).

[25] J. M. Martinis, K. B. Cooper, R. McDermott, M. Steffen, M. Ansmann, K. D. Osborn, K. Cicak, S. Oh, D. P. Pappas, R. W. Simmonds, and C. C. Yu, Phys. Rev. Lett. **95**, 210503 (2005).

[26] P. Kumar, S. Sendelbach, M. Beck, J. Freeland, Z. Wang, H. Wang, C. Yu, R. Wu, D. Pappas, and R. McDermott, arXiv preprint arXiv:1604.00877 (2016).

[27] A. Laucht, J. T. Muhonen, F. A. Mohiyaddin, R. Kalra, J. P. Dehollain, S. Freer, F. E. Hudson, M. Veldhorst, R. Rahman, G. Klimeck, K. M. Itoh, D. N. Jamieson, J. C. McCallum, A. S. Dzurak, and A. Morello, Sci. Adv. **1** (2015).

[28] E. T. Jaynes and F. W. Cummings, Proceedings of the IEEE **51**, 89 (1963).

[29] G. Wolfowicz, S. Simmons, A. M. Tyryshkin, R. E. George, H. Riemann, N. V. Abrosimov, P. Becker, H.-J. Pohl, S. A. Lyon, M. L. W. Thewalt, and J. J. L. Morton, Phys. Rev. B **86**, 245301 (2012).

[9] A. Bienfait, J. J. Pla, Y. Kubo, X. Zhou, M. Stern, C. C. Lo, C. D. Weis, T. Schenkel, D. Vion, D. Esteve, J. J. L. Morton, and P. Bertet, Nature **531**, 74 (2016).

[31] M. H. Mohammady, G. W. Morley, and T. S. Monteiro, Phys. Rev. Lett. **105**, 067602 (2010).

[32] J. Romijn, T. M. Klapwijk, M. J. Renne, and J. E. Mooij, Phys. Rev. B **26**, 3648 (1982).

[33] R. Huebener, R. Kampwirth, R. Martin, T. Barbee, and R. Zubeck, IEEE Trans. Magn. **11**, 344 (1975).

[34] L.-M. Duan, M. Lukin, J. I. Cirac, and P. Zoller, Nature **414**, 413 (2001).

[35] B. Sarabi, A. N. Ramanayaka, A. L. Burin, F. C. Wellstood, and K. D. Osborn, Appl. Phys. Lett. **106**, 172601 (2015).

[36] A. D. O'Connell, M. Ansmann, R. C. Bialczak, M. Hofheinz, N. Katz, E. Lucero, C. McKenney, M. Neeley, H. Wang, E. M. Weig, A. N. Cleland, and J. M. Martinis, Appl. Phys. Lett. **92**, 112903 (2008).

[37] X. Liu, D. R. Queen, T. H. Metcalf, J. E. Karel, and F. Hellman, Phys. Rev. Lett. **113**, 025503 (2014).

Supplementary Material for
"Prospective two orders of magnitude enhancement in direct magnetic coupling of a single-atom spin to a circuit resonator"

Bahman Sarabi[1,2], Peihao Huang[1,2] and Neil M. Zimmerman[1]

[1]*National Institute of Standards and Technology, Gaithersburg, MD 20899, USA*

[2]*Joint Quantum Institute, University of Maryland, College Park, Maryland 20742, USA*

INDUCTANCE SIMULATIONS AND CALCULATIONS

The total inductance $L_\text{tot} = L_\text{g} + L_\text{p}$ within the resonator consists of the geometric inductance L_g of the spiral inductor giving rise to the magnetic field B_ac that couples to the donor electron spin, and parasitic inductance L_p which does not contribute to B_ac and only limits it. L_g consists of the trace inductance L_t arising from the length of the spiral trace, and some mutual inductance L_M between the loops and the spirals, such that $L_\text{g} = L_\text{t} + L_\text{M}$. The parasitic inductance L_p arises from the kinetic inductance of the spiral L_k, kinetic inductance within capacitor plates $L_\text{C,k}$, geometric self-inductance of the capacitor $L_\text{C,g}$, inductance of the uncovered areas of the capacitor plates $L_\text{C,uc}$ and the coupling inductance L_coup, such that $L_\text{p} = L_\text{k} + L_\text{C,k} + L_\text{C,g} + L_\text{C,uc} + L_\text{coup}$. Below, we describe our estimation of all of the aforementioned inductances.

L_g is approximately calculated and also separately simulated. In the calculations, for simplicity, we assume that each loop of the spiral inductor is truly circular and estimate L_g using the geometric mean distance (GMD) method to the second order in the ratio of the conductor diameter to the loop radius [S1]. This independent loop approximation (ILA) ignores the mutual inductance L_M within the spiral loops. However, one should note that L_M contributes to B_ac and is not parasitic. Nevertheless, we simulated the spiral geometry in FastHenry 3-D inductance extraction program [S2], which accounts for the mutual inductances L_M within the spiral geometry. Figure S1 shows a comparison between the simulation and the approximative calculation, where the latter ignores L_M. Clearly, L_M constitutes a larger portion of L_g with increasing N_loops, but is negligible up to the optimum $N_\text{loops} \approx 2, 3$. The total inductance L_tot in Fig. 2(a) is plotted using L_g from FastHenry simulations. However, for simplicity, the ac field contributed by L_M was not taken into account in calculating g, resulting in an underestimated g in Fig. 2(c).
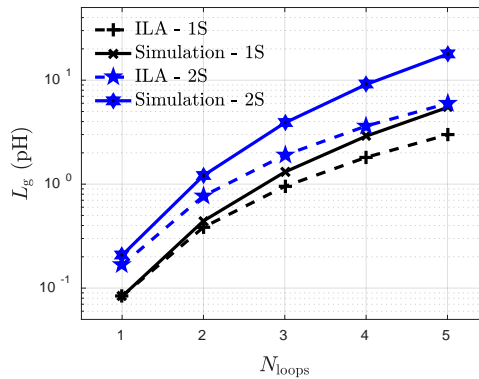

FIG. S1. Comparison between the independent loop approximation (ILA) and FastHenry simulations of the spiral geometric inductance versus for different spiral loop counts N_loops for the double spiral (2S) and single spiral (1S) geometries.

The kinetic inductance L_k of the spiral loop is caused by the kinetic energy of the quasi-particles within the superconductor and hence does not create any magnetic fields. Using the Cooper-pair density n_s and mass m_C for a particular superconducting material, the length of the superconducting line l_s and its cross-sectional area A_s, one can estimate $L_\text{k} = m_\text{C} l_\text{s} / 4 n_\text{s} e^2 A_\text{s}$ [S3], where e denotes the electron charge. The kinetic inductance within the capacitor

plates, $L_{C,k} \approx 60$ fH, is negligible due to the large cross-sectional area of the plates. The geometric self-inductance of the capacitor, calculated using a stripline model, is $L_{C,g} \approx 62$ fH. To confirm this, we simulated the resonator geometry including the capacitor and found $L_{C,g} = 64$ fH, in agreement with the calculated value and also negligible for $N_{loops} \gtrsim 2$. The relatively small $L_{C,g}$ is due to the small capacitor insulating thickness (25 nm). The inductance of the non-overlapping parts of the capacitor plates can however be significant and must be separately taken into account. Assuming 1 μm of completely isolated and uncovered area on the bottom capacitor plate compatible with standard photolithography, we estimate a maximum for this inductance to be $L_{C,uc} \approx 0.8$ pH. However, our simulations showed that due to field distributions interacting with the uncovered area, $L_{C,uc} \approx 6$ fH, two orders of magnitude smaller than the theoretical maximum, and hence negligible. Finally, since any inductive coupling to the resonator results in additional stray inductance in the resonator circuit, we propose a capacitively coupled design allowing us to assume $L_{coup} = 0$. In order to take into account total background parasitic inductance, a conservative value for $L_{C,k} + L_{C,g} + L_{C,uc} + L_{coup} = 0.8$ pH is assumed in Fig. 2. Due to the desired operation frequency $\omega_0 = 1/\sqrt{L_{tot}C}$, this value of inductance is needed (either intentionally or as parasitic inductance) in order to have a reasonably sized capacitor. Here, the assumption of this inductance value being entirely parasitic leads to further underestimation of g.

In order to obtain the desired resonance frequencies with these relatively small inductances, relatively large capacitances are required. By using a capacitor insulator thickness of $d_0 = 25$ nm, we can keep the square-shaped capacitor dimensions below 200 μm, and also suppress capacitor's geometric inductance which contributes to L_p.

A simulation of g as a function of the spiral trace width w, spacing s and thickness t, was performed. By assuming $w = s = t$, the results showed that, for the Nb (Al) set, the optimum g is obtained when 30 nm $\lesssim w = s = t \lesssim 35$ nm ($w = s = t \approx 20$ nm), weakly depending on whether the 1S or the 2S geometry is used. If e-beam lithography resolution of 20 nm is implemented, the Al set can yield a spin-photon coupling rate of $g/2\pi = 0.45$ MHz.

POSSIBILITY OF DONOR IONIZATION

It has been previously shown that the donor can be ionized in the vicinity of metallic or other conductive structures due to energy band bendings [S4]. For Al-Si interface, the relatively small work function difference of -30 meV (4.08 eV for Al and 4.05 eV for Si) is smaller than the donor electron binding energy of -46 meV [S5], and hence using aluminum is expected to allow the donor bound state. However, the Nb work function of 4.3 eV causes significant band bending which can result in donor ionization. By biasing the microwave transmission line and hence the resonator with a DC voltage through C_c and C_{GND}, one can modulate the potential energy arrangement in the neighborhood of the donor and recreate a bound state. If a conduction band electron is required to fill the bound state, solutions such as shining a light pulse using a light emitting diode to create excess electron-hole pairs or using an ohmic path to controllably inject electrons can be employed.

QUBIT OPERATION

The qubit operation parameters of this device are adopted from a commonly used cQED architecture [S6]. To estimate the initialization, manipulation and readout performance, we focus on the Nb/P-2S configuration with $g/2\pi = 0.24$ MHz, a realistic resonator internal quality factor $Q_i = 4 \times 10^4$ and an external quality factor $Q_e = 4 \times 10^5$ easily realizable according to our estimation of capacitive coupling [S7]. We also assume that the resonator frequency and the Zeeman splitting frequency are $\omega_0/2\pi = 5.6$ GHz and $\omega_s/2\pi \approx 5.6$ GHz, respectively. The zero-detuning ($\Delta \equiv \omega_s - \omega_0 = 0$) relaxation time limited by the Purcell effect for this strongly-coupled system is obtained as $T_{1,init} = \Gamma_P^{-1} = 2\kappa^{-1} = 2.3$ μs [S8] which is several orders of magnitude shorter than the free spin relaxation. The linear dependence of Γ_P to κ is a result of strong coupling, which distinguishes it from previously measured weakly coupled systems [S9] where $\Gamma_P \propto \kappa^{-1}$.

For spin manipulation, we can Stark shift the spin states using the electrodes shown in Figs. 1(b)-(d), or use magnetic field tuning the perturb the Zeeman energy. For a demonstration of the qubit operation parameters of the device, we chose to operate at $\Delta = 40g$, where the strong-coupling Purcell rate becomes $\Gamma_P/2\pi = \frac{1}{4\pi}(\kappa - \sqrt{2}\sqrt{-A + \sqrt{A^2 + \kappa^2\Delta^2}}) = 88$ Hz with $A \equiv \Delta^2 + 4g^2 - \kappa^2/4$ [S8], giving rise to $T_{2,rot} = 2/\Gamma_P = 1.8$ ms. This relaxation time is not far from the measured Hahn-Echo $T_2^H = 1.1$ ms for a P donor electron spin in enriched ^{28}Si, believed to be limited primarily by the static magnetic field noise and thermal noise and not due to the proximity to the oxide layers or other amorphous material [S10]. Therefore, it is reasonable to assume that the spin T_2 time in our device is Purcell limited, hence set by $T_{2,rot}$. Note that for the Al/Bi set, the direction of the Stark shift

must be such that the $|F, m_F\rangle = |5, -5\rangle \leftrightarrow |4, -4\rangle$ transition frequency, already reduced by a relatively small B_0 to lift the multiplet degeneracy, is further reduced to avoid exciting the higher frequency multiplet transitions. In this detuned qubit control regime, the microwave drive frequency is $\omega_{\mu w}/2\pi = \omega_s/2\pi + (2n_{\lim} + 1)g^2/2\pi\Delta = 5.614406$ GHz where photon number $n_{\lim} = \Delta^2/4g^2 = 400$ sets the maximum drive power [S6], and is lower than the critical photon number $n_{\rm crit} \approx 1800$ corresponding to the spiral inductor's critical current. The qubit rotation speed, at on-resonance photon number $n_{\rm res} \approx 17 \times 10^6$ set by $n_{\lim}$ and $\omega_{\mu w}$, is $f_{\rm rot} = g\kappa\sqrt{n_{\rm res}}/\pi\Delta = 29$ MHz [S11], corresponding to $N_\pi = 2f_{\rm rot}T_{2,\rm rot} > 10^5$ coherent π-rotations.

The spin readout also occurs in the same detuned regime, where cavity frequency is "pulled" giving rise to a $f_{sep} = g^2/\pi\Delta = 12$ kHz separation frequency depending on the spin state. This corresponds to a phase shift of $\phi = 2\arctan(2g^2/\kappa\Delta) = 10°$, well above the measurement sensitivity usually considered to be $0.1°$. The measurement time to resolve ϕ is estimated to be $T_m = (2\kappa N_{\rm read}\theta_0^2)^{-1} = 3.1$ μs where $\theta_0 \equiv 2g^2/\kappa\Delta$ [S6] and $N_{\rm read} = 25$ is the readout photon number (we must use $N_{\rm read} < \Delta^2/4g^2$).

———————

[S1] F. W. Grover, *Inductance calculations: working formulas and tables* (Courier Corporation, 2004).

[S2] M. Kamon, M. J. Tsuk, and J. K. White, IEEE Transactions on Microwave theory and techniques **42**, 1750 (1994).

[S3] M. Tinkham, *Introduction to superconductivity* (Courier Corporation, 1996).

[S4] M. Fuechsle, J. A. Miwa, S. Mahapatra, H. Ryu, S. Lee, O. Warschkow, L. C. L. Hollenberg, G. Klimeck, and M. Y. Simmons, Nat. Nanotechnol. **7**, 242 (2012).

[S5] C. Jagannath, Z. W. Grabowski, and A. K. Ramdas, Phys. Rev. B **23**, 2082 (1981).

[S6] A. Blais, R.-S. Huang, A. Wallraff, S. M. Girvin, and R. J. Schoelkopf, Phys. Rev. A **69**, 062320 (2004).

[S7] J. M. Martinis, R. Barends, and A. N. Korotkov, arXiv preprint arXiv:1410.3458 (2014).

[S8] E. A. Sete, J. M. Gambetta, and A. N. Korotkov, Phys. Rev. B **89**, 104516 (2014).

[S9] A. Bienfait, J. J. Pla, Y. Kubo, X. Zhou, M. Stern, C. C. Lo, C. D. Weis, T. Schenkel, D. Vion, D. Esteve, et al., Nature **531**, 74 (2016).

[S10] J. T. Muhonen, J. P. Dehollain, A. Laucht, F. E. Hudson, R. Kalra, T. Sekiguchi, K. M. Itoh, D. N. Jamieson, J. C. McCallum, A. S. Dzurak, et al., Nat. Nanotechnol. **9**, 986 (2014).

[S11] S. Haroche, in *Fundamental Systems in Quantum Optics* (Elsevier Science Publishers B.V., 1993).